

Structural Gaussian Priors for Bayesian CT reconstruction of Subsea Pipes

Silja W. Christensen, Nicolai A. B. Riis, Felipe Uribe, and Jakob S. Jørgensen

Department of Applied Mathematics and Computer Science, Technical University of Denmark, Kongens Lyngby, Denmark

E-mail: swech@dtu.dk

Abstract. A non-destructive testing (NDT) application of X-ray computed tomography (CT) is inspection of subsea pipes in operation via 2D cross-sectional scans. Data acquisition is time-consuming and costly due to the challenging subsea environment. Reducing the number of projections in a scan can yield time and cost savings, but compromises the reconstruction quality, if conventional reconstruction methods are used. In this work we take a Bayesian approach to CT reconstruction and focus on designing an effective prior to make use of available structural information about the pipe geometry. We propose a new class of *structural Gaussian priors* to enforce expected material properties in different regions of the reconstructed image based on independent Gaussian priors in combination with global regularity through a Gaussian Markov Random Field (GMRF) prior. Numerical experiments with synthetic and real data show that the proposed structural Gaussian prior can reduce artifacts and enhance contrast in the reconstruction compared to using only a global GMRF prior or no prior at all. We show how the resulting posterior distribution can be efficiently sampled even for large-scale images, which is essential for practical NDT applications.

1. Introduction

Subsea pipelines are used to transport oil and gas around the world. It is crucial that the subsea pipes are in good condition to avoid environmentally damaging leaks. Therefore, efficient methods for non-destructive inspection are in demand. One suitable method is X-ray computed tomography (CT) that is used to obtain 2D cross sectional images of the pipes. In order to produce high quality images with limited noise and artifacts, standard CT reconstruction methods require lengthy measurements at many projection (view) angles. To reduce costs, it is desirable to limit measurement time, which can be done by reducing the number of view angles. However, this compromises the reconstruction quality significantly, if standard iterative methods are used. Moreover, due to scarce and noisy data, there is significant uncertainty affecting the reconstructions. Therefore, we propose a Bayesian approach, where a-priori knowledge of the pipes' internal structure improves the image reconstruction quality even for cases with measurements taken at few view angles.

Previous work has taken a deterministic approach to CT scanning of subsea pipes [1]. They use microlocal analysis to design a favorable offset scan geometry and propose a reconstruction method based on shearlets with a weighted sparsity penalty. However, to account for and quantify uncertainty in the reconstructions, a Bayesian approach is needed for the CT problem.

In Bayesian CT reconstruction [2, 3, 4], it is important to choose an appropriate prior. Typical choices in this setting are Markov Random Field (MRF) priors given by multivariate Gaussian and Laplacian distributions. This is because they represent a statistical parallel to the well-known Tikhonov and total variation (TV) regularization methods, which are commonly used in the field of inverse problems and in particular CT [5, 6]. An overview of several MRF type priors applied to 2D inverse problems (including CT) is given in [7] and more detailed descriptions can be found in earlier papers [8, 9]. A recent approach is the Cauchy differences prior (also a MRF-type prior), which is edge-preserving and discretization invariant [10]. All the MRF priors have regularizing effects, and depending on the scanned object, a smoothness-promoting or edge-preserving prior can be chosen. A common characteristic for these priors is that they cannot model specific features such as the layer structure in subsea pipes.

If a particular structure is known in advance, a stronger prior can be formed. A series of studies use this idea by forming a texture-preserving prior for low-dose CT reconstruction using a previous normal-dose scan [11, 12, 13, 14]. Another study exploits the fact that the human body consists of a finite number of tissue types with well-known attenuation coefficients and designs the prior accordingly including an inherent classification problem [15].

The driving idea in this work is to utilize as much a-priori information as possible. We know the overall layout of the pipes because they are manufactured according to specific design standards. This leads to our proposed *structural Gaussian prior* that introduces information about the pipes' layered structure as well as the constitutive materials. Numerical experiments show that this prior improves the reconstruction quality compared to standard iterative methods, especially if only few view angles are available. Moreover, the probabilistic approach allows a high degree of freedom in modelling noise and a-priori information, and through posterior sampling we can obtain reconstructions with uncertainty estimates. Another advantage of the structural Gaussian prior is that it can be sampled reliably and efficiently in large-scale problems.

Our paper is organized as follows. In Section 2 we introduce the Bayesian approach to CT reconstruction. Section 3 describes our proposed structural Gaussian prior. In Section 4 we derive the posterior and how to sample it efficiently. In Section 5 we perform numerical experiments with synthetic and real data and in Section 6 we discuss and conclude our findings.

2. Bayesian CT problem

Deep sea oil pipes are large and consist of dense materials including steel and concrete. In order to penetrate the pipe with X-rays, it is necessary to use high power and a narrow beam source. The narrow beam can not illuminate the full pipe, but an exterior tomography setup can be used, where the X-ray source is offset from the pipe centre, which is also the rotation axis. Microlocal analysis shows that this setup is ideal, if we are interested in recovering the pipe and defects therein rather than the center of the pipe [1]. We use real data acquired from a prototype set-up of an oil pipe CT scanner. A detector panel with 510 sensors of sizes 0.8 mm each was used, and 360 equi-angular projections were recorded in a full 360 degree rotation. The pipe, its specifications, and the offset fan-beam acquisition geometry are illustrated in Figure 1.

2.1. CT model

If we discretize the reconstruction domain in pixels, the inverse problem associated with CT can be expressed as a linear system of equations,

$$\mathbf{d} = \mathbf{Ax} + \mathbf{e}, \quad \mathbf{e} \sim \mathcal{N}\left(\mathbf{0}, \frac{1}{\lambda} \mathbf{I}_n\right), \quad (1)$$

where $\mathbf{d} \in \mathbb{R}^m$ is the observed X-ray absorption (known as a sinogram), $\mathbf{x} \in \mathbb{R}^n$ is the unknown vector of linear attenuation coefficients in the reconstruction domain with $N \times N = n$ pixels, and

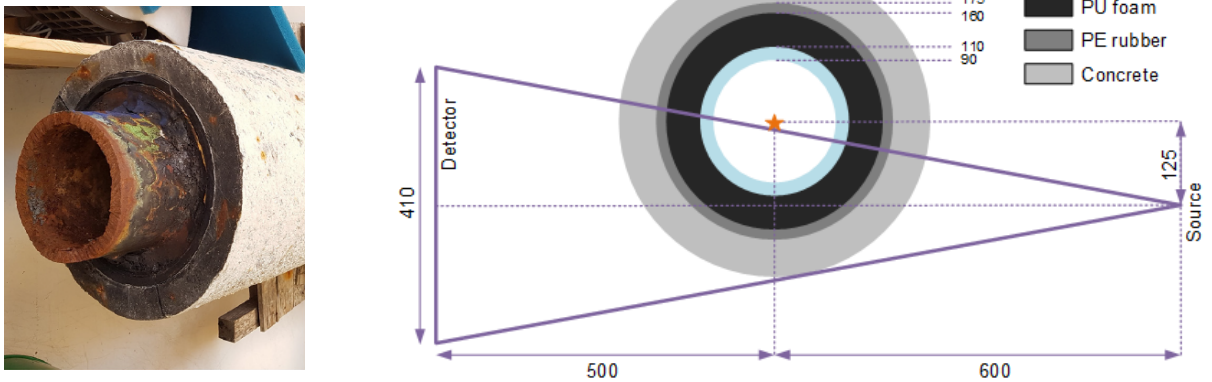


Figure 1. *Left:* Photograph of subsea oil pipe. *Right:* Pipe and offset scan geometry specifications; dimensions in mm. The CT rotation axis is marked with a star.

$\mathbf{A} \in \mathbb{R}^{m \times n}$ contains entries a_{ij} that describe the intersection of ray i with pixel j (see, e.g., [5] for details). We model the data noise as additive Gaussian, because of the high-intensity X-rays used in the data collection process. That is, $\mathbf{e} \in \mathbb{R}^m$ is independent and identically distributed Gaussian noise with mean zero and precision parameter λ , and $\mathbf{I}_n \in \mathbb{R}^{n \times n}$ is an identity matrix.

2.2. Bayesian inversion

We take a Bayesian approach to the CT problem. Using Bayes' Theorem we can characterize the solution in terms of the posterior distribution given by the probability density function (PDF),

$$\pi_{\text{post}}(\mathbf{x} | \mathbf{d}) \propto \pi_{\text{pr}}(\mathbf{x}) \pi(\mathbf{d} | \mathbf{x}). \quad (2)$$

Here, $\pi_{\text{pr}}(\mathbf{x})$ is the PDF of the prior distribution describing some known properties of the attenuation coefficients \mathbf{x} . The prior is modelled as a Gaussian distribution with PDF given by

$$\pi_{\text{pr}}(\mathbf{x}) = \frac{1}{(2\pi)^{n/2}} (|\mathbf{R}^T \mathbf{R}|)^{1/2} \exp\left(-\frac{1}{2} \|\mathbf{R}(\mathbf{x} - \boldsymbol{\mu})\|_2^2\right), \quad (3)$$

where $\boldsymbol{\mu} \in \mathbb{R}^n$ is the mean and $(\mathbf{R}^T \mathbf{R}) \in \mathbb{R}^{n \times n}$ the precision matrix with full rank. We refer to \mathbf{R} as the square-root precision matrix, and $|\cdot|$ is a matrix determinant. Below, in Section 3, the specifics of how we build the pipe structure into the Gaussian prior are given.

From (1), we obtain the distribution of the data \mathbf{d} given some known image \mathbf{x} ,

$$\pi(\mathbf{d} | \mathbf{x}) = \left(\frac{\lambda}{2\pi}\right)^{m/2} \exp\left(-\frac{\lambda}{2} \|\mathbf{A}\mathbf{x} - \mathbf{d}\|_2^2\right), \quad (4)$$

which can be seen as the likelihood function of \mathbf{x} given some observed data \mathbf{d} .

Because the prior and likelihood are Gaussian, we can obtain a closed-form expression for the posterior, which is also Gaussian (see Section 4.1). It is numerically impractical to compute the posterior precision matrix, but we will see, that the posterior mean is simple to obtain. Because the distribution is Gaussian, the mean is equivalent to the maximum a-posteriori probability (MAP) estimate, which often used in the literature to describe the posterior. But this does not realize the full potential of the Bayesian approach. One of the strong points of Bayesian inversion is the ability to give uncertainty estimates. Therefore, our approach entails a method for sampling the posterior distribution as described in Section 4.2.

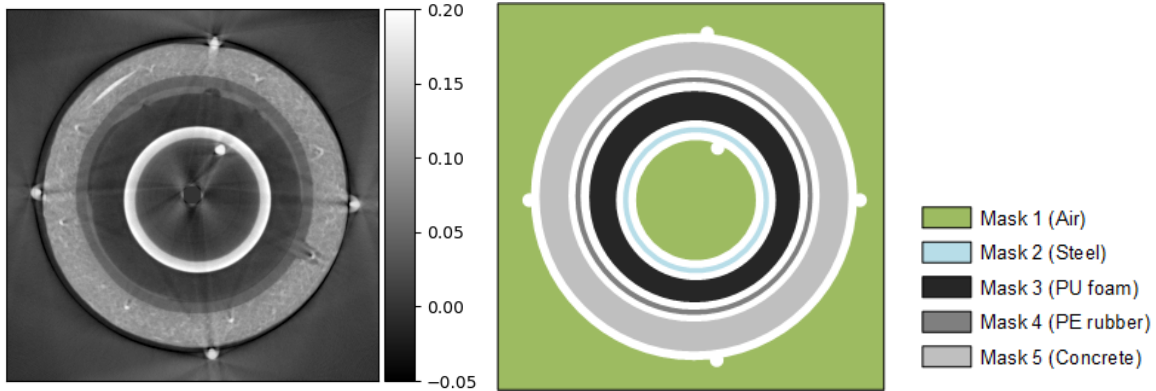


Figure 2. *Left:* Real pipe with four layers of different materials and a background of air. *Right:* SGP masks for $i = 1, \dots, 5$ that each represents a material with attenuation coefficient α_i given in (5). The white regions do not have any prior promoting specific attenuation coefficients. The index $i = 0$ is used to denote the prior on the whole image domain (background and pipe).

3. Structural Gaussian priors

We must specify a prior in order to perform Bayesian CT reconstruction. We work with Gaussian priors because they have nice mathematical properties making them easy to combine, and because they can be sampled efficiently. First, we outline the a-priori structural information that we have. Then we describe our proposed method of incorporating the known pipe geometry into what we call *structural Gaussian priors (SGPs)*. The SGP combines (stacks) priors for each of the materials in the pipe enforcing a different prior in each region. In addition to the pipe material and geometry information, the SGP also contains a prior on the pixel differences of the whole image. The purpose of this is to add a global smoothness assumption on the image, which also ensures full rank of the precision matrix of the combined Gaussian prior in (3).

3.1. A-priori structural information

We have a-priori information about the pipe's layered structure and constitutive materials, which we will incorporate in the prior model. This is the core idea of our proposed SGP. To build the SGP we need: 1) Masks for each pipe layer and for the background, and 2) estimates of the linear attenuation coefficients of the layer materials.

3.1.1. Pipe layer masks Given p non-overlapping regions of different materials, we represent each region by a mask, i.e., a binary vector \mathbf{m}_i for $i = 1, \dots, p$, the same size as the image \mathbf{x} in which the value of element j is 1 if pixel j is in region i and 0 if not. Figure 2 shows a reconstruction of the real pipe and the corresponding masks (with $p = 5$). We use masks that are slightly smaller than the actual pipe layers to account for modelling error in the pipe structure and scan geometry. The masks are constructed based on a high-quality standard CT reconstruction of the real pipe, this may also be obtained from lower-quality data or e.g. from CAD drawings. We further define mask matrices $\mathbf{M}_i \in \mathbb{R}^{l_i \times n}$, $i = 1, \dots, p$, that pick out the l_i pixels of region i of the n -dimensional image. Specifically, \mathbf{M}_i is formed by keeping only the l_i rows of \mathbf{I}_n indexed by 1-values in the mask \mathbf{m}_i .

3.1.2. Linear attenuation coefficients of pipe materials When the X-ray energy is known, we can estimate the linear attenuation coefficients α_i (ignoring scattering) for the materials as [16]:

$$\alpha_i = \kappa_i(E)\rho_i, \quad i = 1, \dots, p, \quad (5)$$

where ρ_i is the material density and $\kappa_i(E)$ is the mass attenuation coefficient at X-ray energy E that can be found, e.g., in the NIST database [17].

3.2. Structural Gaussian priors

To form the SGP we use Gaussian distributions defined in terms of means $\boldsymbol{\mu}_i \in \mathbb{R}^{l_i}$ and a symmetric positive semi-definite precision matrices $(\mathbf{R}_i^T \mathbf{R}_i) \in \mathbb{R}^{n \times n}$. In (3) we gave an expression for Gaussians with precision matrices of full rank. When forming the SGP we will need intrinsic Gaussians, that are also defined for rank deficient precision matrices of rank $n - k > 0$. The intrinsic Gaussian prior density is given [18, Ch. 3]:

$$\pi_i(\mathbf{x}) = \frac{1}{(2\pi)^{(n-k)/2}} \left(|\mathbf{R}_i^T \mathbf{R}_i|^* \right)^{1/2} \exp \left(-\frac{1}{2} \|\mathbf{R}_i(\mathbf{x} - \boldsymbol{\mu}_i)\|_2^2 \right), \quad (6)$$

where $|\cdot|^*$ is a generalized determinant given by the product of the $n - k$ non-zero eigenvalues of the precision matrix. Note this density is multivariate Gaussian if and only if $k = 0$. In the SGP, we use two different Gaussian priors that are specified below:

IID: The independent and identically distributed (IID) Gaussian prior is a noise dampening prior that favors posterior pixel values around the prior mean. We use it to express a-priori information of expected linear attenuation coefficients α_i in the p different materials. The prior is defined as an intrinsic Gaussian parameterized by mean and square-root precision:

$$\boldsymbol{\mu}_i = \alpha_i \mathbf{1} \quad \text{and} \quad \mathbf{R}_i = \sqrt{\delta_i} \mathbf{M}_i, \quad (7)$$

where $\mathbf{1} \in \mathbb{R}^{l_i}$ is a vector of ones and δ_i is a prior precision parameter.

GMRF: The Gaussian Markov Random Field (GMRF) prior is a smoothing prior that promotes neighbouring pixels to take the same value. The pipe materials can be considered roughly homogeneous and therefore the GMRF prior is enforced on the entire image domain. We index this prior with $i = 0$ corresponding to the whole image and in this case the mean and square-root precision are:

$$\boldsymbol{\mu}_0 = \mathbf{0}, \quad \text{and} \quad \mathbf{R}_0 = \sqrt{\delta_0} \begin{bmatrix} \mathbf{D}_1 \\ \mathbf{D}_2 \end{bmatrix}, \quad (8)$$

where $\mathbf{0} \in \mathbb{R}^n$ is a vector of zeros, $\mathbf{D}_1 = \mathbf{I}_N \otimes \mathbf{D}$, $\mathbf{D}_2 = \mathbf{D} \otimes \mathbf{I}_N$, and $\mathbf{D} \in \mathbb{R}^{(N+1) \times N}$ is a finite difference matrix with backward differences and zero Dirichlet boundary conditions, and \otimes denotes the Kronecker product. Note that \mathbf{R}_0 has full column rank. Then, the precision matrix has full rank, and the density is thus multivariate Gaussian.

To build the SGP prior, we enforce IID priors on the masked image regions and a GMRF prior on the whole image domain as described above. Under the assumption that the priors $\pi_i(\mathbf{x})$, $i = 0, \dots, p$ are independent of each other, the SGP prior is a product of the individual priors:

$$\pi_{\text{pr}}(\mathbf{x}) = \prod_{i=0}^p \pi_i(\mathbf{x}). \quad (9)$$

Then, the prior mean and square-root precision are given:

$$\mathbf{R}_{\text{pr}} = \begin{bmatrix} \mathbf{R}_0 \\ \vdots \\ \mathbf{R}_p \end{bmatrix} \quad \text{and} \quad \boldsymbol{\mu}_{\text{pr}} = (\mathbf{R}_{\text{pr}}^T \mathbf{R}_{\text{pr}})^{-1} \sum_{i=0}^p \mathbf{R}_i^T \mathbf{R}_i \boldsymbol{\mu}_i. \quad (10)$$

Note, that the full column rank of \mathbf{R}_0 leads to \mathbf{R}_{pr} also having full column rank, and therefore the prior precision matrix $\mathbf{R}_{\text{pr}}^T \mathbf{R}_{\text{pr}}$ has full rank and is invertible.

3.2.1. SGP configurations We use the pipe shown in Figure 2 as a case study for numerical experiments in Section 5. The pipe consists of four different materials, steel in region 2, PU foam in region 3, PE rubber in region 4, and concrete in region 5. The pipe is scanned with air as the background and this will be denoted region 1. Thus we have $p = 5$ masked regions where we can impose IID priors promoting the expected attenuation coefficients. We study two configurations of the SGP:

SGP-BG: Assuming we have information about the pipe's dimensions but not internal structure, we use a GMRF on the whole domain and add an IID prior on the air background (“BG”) such that $\pi_{\text{pr}}(\mathbf{x}) = \prod_{i=0}^1 \pi_i(\mathbf{x})$.

SGP-F: Assuming we also have information about the internal pipe structure, we again use a GMRF on the full (“F”) domain and add IID priors on the background and on the pipe layers such that $\pi_{\text{pr}}(\mathbf{x}) = \prod_{i=0}^5 \pi_i(\mathbf{x})$.

4. Gaussian posterior and efficient sampling

In Sections 2 and 3 we assumed Gaussian distributions for the likelihood and priors respectively, which in turn yields a Gaussian posterior PDF [2]. This is mathematically convenient because we can derive a closed-form expression for this distribution and sample it efficiently. Below we give the posterior PDF and then show how to sample it by solving a system of linear equations.

4.1. Posterior PDF

The posterior PDF is given by:

$$\begin{aligned} \pi_{\text{post}}(\mathbf{x} | \mathbf{d}) &\propto \left(\frac{\lambda}{2\pi}\right)^{\frac{m}{2}} \exp\left[-\frac{\lambda}{2} \|\mathbf{Ax} - \mathbf{d}\|_2^2\right] \times \prod_{i=0}^p \left(\left|\frac{\mathbf{R}_i^T \mathbf{R}_i}{2\pi}\right|^*\right)^{\frac{1}{2}} \exp\left[-\frac{1}{2} \|\mathbf{R}_i(\mathbf{x} - \boldsymbol{\mu}_i)\|_2^2\right] \\ &\propto \exp\left[-\frac{\lambda}{2} \|\mathbf{Ax} - \mathbf{d}\|_2^2 - \frac{1}{2} \sum_{i=0}^p \|\mathbf{R}_i(\mathbf{x} - \boldsymbol{\mu}_i)\|_2^2\right]. \end{aligned} \quad (11)$$

The above expression defines the Gaussian random vector

$$\mathbf{x} | \mathbf{d} \sim \mathcal{N}(\boldsymbol{\mu}_{\text{post}}, (\mathbf{R}_{\text{post}}^T \mathbf{R}_{\text{post}})^{-1}), \quad (12)$$

where the posterior square-root precision is given by

$$\mathbf{R}_{\text{post}} = \begin{bmatrix} \sqrt{\lambda} \mathbf{A} \\ \mathbf{R}_0 \\ \vdots \\ \mathbf{R}_p \end{bmatrix} \in \mathbb{R}^{(m+2N(N+1)+\sum_{i=1}^p l_i) \times n}, \quad (13)$$

and the posterior mean is given implicitly by the expression:

$$\mathbf{R}_{\text{post}}^T \mathbf{R}_{\text{post}} \boldsymbol{\mu}_{\text{post}} = \lambda \mathbf{A}^T \mathbf{d} + \sum_{i=0}^p \mathbf{R}_i^T \mathbf{R}_i \boldsymbol{\mu}_i. \quad (14)$$

Since \mathbf{R}_0 and \mathbf{R}_{post} have full column rank, the posterior precision is invertible, and the posterior distribution is Gaussian with well-defined covariance. That is, the closed-form expression for the posterior distribution is (12), which can be seen by factoring out (11) and reordering the equation into the form (3).

The large-scale nature of CT makes it infeasible to form the matrix \mathbf{A} explicitly, which is avoided by matrix-free implementations of the application of \mathbf{A} and its adjoint. Then, the posterior mean can be obtained by solving (14). However, to compute the posterior precision we must form $\mathbf{A}^T \mathbf{A}$, making it numerically impractical. Instead we sample the posterior as described below, and statistics of the samples are used to obtain an uncertainty estimate.

4.2. Posterior Sampling

Our goal is to efficiently sample the posterior (12) without explicitly forming the matrix \mathbf{A} . Inspired by [4], we generate posterior realizations by solving the linear system of equations:

$$\mathbf{R}_{\text{post}} \mathbf{x}^* = \begin{bmatrix} \sqrt{\lambda} \mathbf{d} \\ \mathbf{R}_0 \boldsymbol{\mu}_0 \\ \vdots \\ \mathbf{R}_p \boldsymbol{\mu}_p \end{bmatrix} + \boldsymbol{\xi}, \quad \boldsymbol{\xi} \sim \mathcal{N}(\mathbf{0}, \mathbf{I}_{m+2N(N+1)+\sum_{i=1}^p l_i}). \quad (15)$$

Note that the solution method must support matrix-free implementation of \mathbf{A} .

We can show that \mathbf{x}^* is distributed according to the posterior by first forming the normal equations for the linear system above, i.e.

$$\left(\lambda \mathbf{A}^T \mathbf{A} + \sum_{i=0}^p \mathbf{R}_i^T \mathbf{R}_i \right) \mathbf{x}^* = \lambda \mathbf{A}^T \mathbf{d} + \sum_{i=0}^p \mathbf{R}_i^T \mathbf{R}_i \boldsymbol{\mu}_i + \mathbf{R}_{\text{post}}^T \boldsymbol{\xi}. \quad (16)$$

Inserting (13) and solving for \mathbf{x}^* we find

$$\begin{aligned} \mathbf{x}^* &= (\mathbf{R}_{\text{post}}^T \mathbf{R}_{\text{post}})^{-1} \left(\lambda \mathbf{A}^T \mathbf{d} + \sum_{i=0}^p \mathbf{R}_i^T \mathbf{R}_i \boldsymbol{\mu}_i \right) + (\mathbf{R}_{\text{post}}^T \mathbf{R}_{\text{post}})^{-1} \mathbf{R}_{\text{post}}^T \boldsymbol{\xi} \\ &= \boldsymbol{\mu}_{\text{post}} + \mathbf{R}_{\text{post}}^\dagger \boldsymbol{\xi}. \end{aligned} \quad (17)$$

where $\mathbf{R}_{\text{post}}^\dagger = (\mathbf{R}_{\text{post}}^T \mathbf{R}_{\text{post}})^{-1} \mathbf{R}_{\text{post}}^T$ is the Moore–Penrose pseudoinverse. Note that \mathbf{x}^* is a linear transformation of the Gaussian random variable $\boldsymbol{\xi}$. As \mathbf{R}_0 has full column rank $\mathbf{R}_{\text{post}}^\dagger$ has full row rank. It follows [19] that \mathbf{x}^* is Gaussian distributed with mean and covariance:

$$\mathbb{E}(\mathbf{x}^*) = \boldsymbol{\mu}_{\text{post}} + \mathbf{R}_{\text{post}}^\dagger \mathbf{0} = \boldsymbol{\mu}_{\text{post}} \quad (18a)$$

$$\text{Cov}(\mathbf{x}^*) = \mathbf{R}_{\text{post}}^\dagger \mathbf{I} (\mathbf{R}_{\text{post}}^\dagger)^T = (\mathbf{R}_{\text{post}}^T \mathbf{R}_{\text{post}})^{-1}. \quad (18b)$$

This confirms that \mathbf{x}^* is distributed according to the posterior distribution (12). That is, by solving (15) we obtain samples of CT reconstruction images distributed according to (12).

5. Numerical Experiments

FORCE Technology¹ has provided CT data from a deep sea oil pipe acquired in a laboratory experiment using the offset fan-beam scan geometry illustrated in Figure 1. We conduct synthetic and real data CT experiments to assess the performance of the proposed SGPs for obtaining useful CT reconstructions and relevant uncertainty estimates. The results are compared to a conventional deterministic reconstruction method where (1) is solved with the CGLS algorithm and stopped at semi-convergence. We interpret the posterior mean as the CT reconstruction and the posterior 95% credible interval as an associated uncertainty estimate.

5.1. Data description

5.1.1. Phantom Based on the known pipe structure and materials given in Figure 2, we construct a phantom and corresponding SGP mask to perform synthetic experiments (see Figure 3). To avoid inverse crime, the phantom is defined on a 1024×1024 pixel image and the reconstruction is performed on a 512×512 pixel image that represents a 55×55 cm domain

¹ <https://forcetechnology.com/>

i	Material	$\kappa[\text{cm}^2/\text{g}]$	$\rho[\text{g}/\text{cm}^3]$	$\alpha[\text{cm}^{-1}]$
1	Air	0.044	0.0012	~ 0
2	Steel	0.042	7.9	0.16
3	PU foam	0.051*	0.15	0.0077
4	PE rubber	0.051	0.94	0.048
5	Concrete	0.046	2.3	0.11

Table 1. Best estimates and probable ranges for the material constants at beam intensity 2 MeV. *Estimated by PE rubber’s κ due to missing value in database.

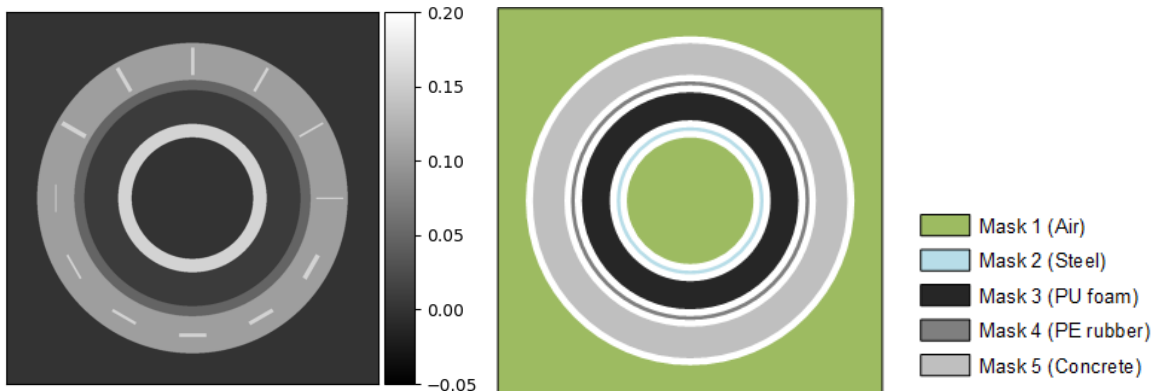


Figure 3. *Left:* Pipe phantom. *Right:* SGP masks for $i = 1, \dots, 5$ that each represents a material with attenuation coefficient α_i given in Table 1. The white regions do not have any prior promoting specific attenuation coefficients. The index $i = 0$ is used to denote the prior on the whole image domain (background and pipe).

leading to pixels of size $\sim 1 \times 1$ mm. The linear attenuation coefficients in each pipe layer are computed according to (5) and with material constants from the NIST database [17], assuming a monochromatic beam of (mean) energy 2 MeV. The beam intensity is an estimate (in fact it is a spectrum), but around these energies the mass attenuation coefficients do not vary significantly. Therefore, we expect the computed linear attenuation coefficients are good estimates and they are listed in Table 1. Note also that we add steel inclusions in the phantom’s concrete layer to simulate steel reinforcement bars in the real pipe. The inclusions are in the radial or tangential directions and their widths are varied from 2-7 mm. With the offset scan geometry, no X-rays will be parallel to near-radial edges, and therefore we expect that the radial inclusions are more difficult to reconstruct than the tangential (see e.g. the discussion in [1] for more details).

5.1.2. Sinograms Using the pipe phantom, offset acquisition geometry, and 2% noise level (i.e. $\|\mathbf{e}\|_2/\|\mathbf{Ax}\|_2 \sim 2\%$), we simulate a 360 view angle sinogram. Assuming the real sinogram has an equivalent noise distribution, we compare the synthetic and real data (Figure 4). Five bands in the sinograms mark the centre region, steel, PE, PU, and concrete layers in that order from the bottom of the sinograms. The bands in the real data sinogram follow sinusoidal curves because the pipe center did not coincide with the rotation center, and the phases of the sinusoidal bands vary because the pipe layers are not completely concentric. The overall similarity between the real data and synthetic data sinograms indicates that our phantom is realistic and the scan geometry close to the real setup. For sparse view angle experiments we simulate data with only 50%, 20% or 10% of the total view angles in the sinograms. Note, that because we reconstruct on a 512×512 pixel image, the CT problem is under-determined in all our experiments.

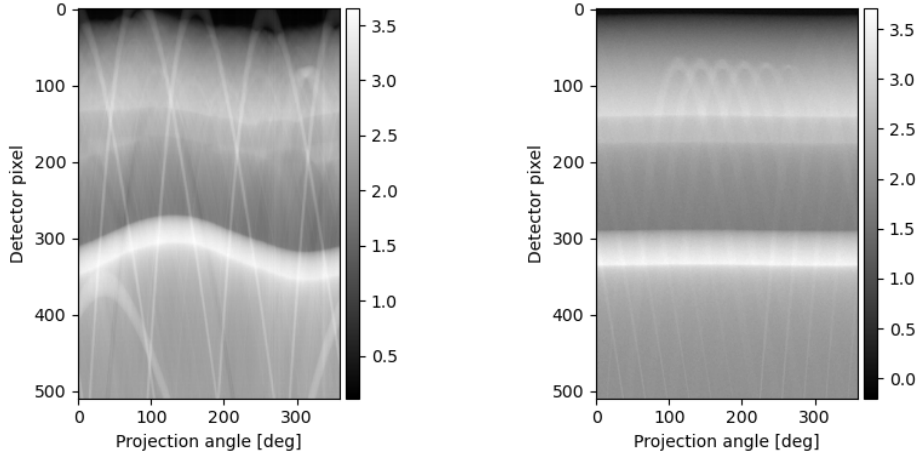


Figure 4. *Left:* Real subsea pipe sinogram. *Right:* Synthetic sinogram with 2% added noise.

5.2. Numerical implementation

5.2.1. Bayesian parameter tuning The posterior in (11) requires choosing several parameters. The data noise of 2% corresponds to a precision parameter $\lambda \approx 400$. The SGP includes several IID Gaussians for which we must determine mean and precision parameters. The means are defined as the estimated linear attenuation coefficients α_i for each pipe material seen in Table 1. The IID Gaussian precision parameters are chosen heuristically such that the priors cover reasonable intervals around the estimated linear attenuation coefficients, representing some uncertainty in the estimates. We expect steel reinforcement bars in the concrete layer, so the precision parameter is reduced here to allow a large range of possible values. Hence, the chosen precision parameters are: $\delta_1 = \delta_2 = \delta_3 = \delta_4 = 1000$, and $\delta_5 = 500$. The final parameter choice is the GMRF precision δ_0 . If we fix all other precision parameters, we can perform a parameter sweep for δ_0 values and choosing the value that minimizes the root-mean-square-error (RMSE) with respect to the synthetic ground truth. An example of δ_0 tuning can be seen in Figure 5 (left). We transfer the GMRF precision choices from the synthetic to the real data case, and check qualitatively that the corresponding reconstructions are acceptable.

5.2.2. Sampling algorithm We use the conjugate gradient least-squares (CGLS) algorithm [20, Ch. 7] to solve (14) for MAP estimates of the posterior and to solve (15) for realizations of the posterior. With this approach we avoid forming and solving the normal equations. Furthermore, this algorithm supports matrix-free implementation of \mathbf{A} as required. We use the ASTRA toolbox to define the CT system and perform matrix-free, efficient, and GPU accelerated forward- and backprojection [21, 22, 23].

If the CGLS algorithm is run until convergence when solving (15), we obtain independent realizations of the posterior (12). However, in order to reduce computation time we employ warm-start by using the previous posterior realization as a starting guess, and we fix the number of iterations to 10 per realization. This approach makes a burn-in phase necessary, i.e. initial samples are discarded. Furthermore, the independency of the samples might be compromised, so we monitor integrated autocorrelation time (IACT) [7, p. 99], which is a measure of correlation in the chains. If $\text{IACT} \approx 1$, we have approximately independent samples.

5.3. Synthetic experiments

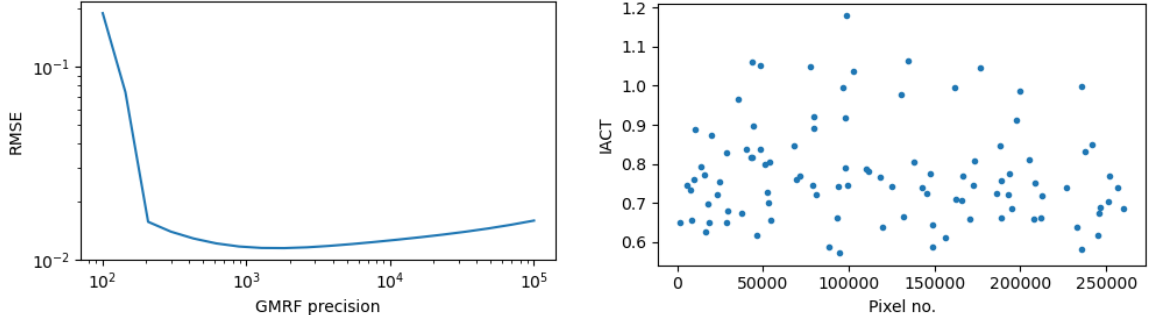


Figure 5. *Left:* Example of GMRF precision parameter sweep from the synthetic experiment. From this, we choose $\delta_0 = 1000$ near the minimum. *Right:* Examples of integrated autocorrelation time (IACT) for 100 randomly selected pixel chains.

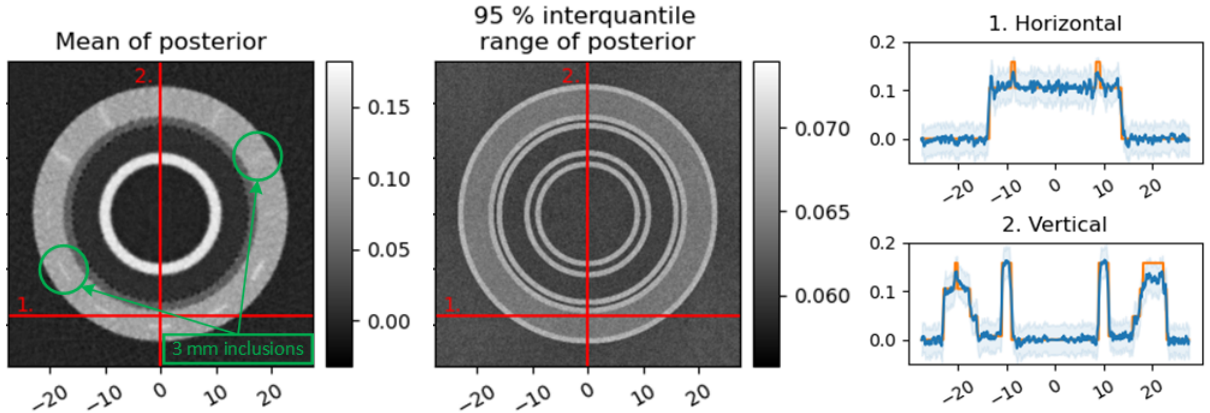


Figure 6. Synthetic test case with 20% view angles and SGP-F prior. *Left, center:* 2D images of the posterior mean and 95% interquartile range. *Right:* 1D slices of posterior mean (blue line) and 95% credibility interval (blue shade), compared to ground truth (orange).

5.3.1. Example of Bayesian inversion with SGP prior We consider a sparse-angle case of only 72 (20%) equi-angular projections out of the original 360. We apply the SGP-F prior to the Bayesian inverse problem. First we tune the GMRF precision parameter as described above in Section 5.2.1. Figure 5 (left) illustrates the parameter sweep, and we choose $\delta_0 = 1000$, where the RMSE is near a minimum. Then, we compute 3000 samples from the posterior as described in Section 5.2.2 and discard the first 1000 as burn-in. We compute IACT for 100 randomly selected pixel chains and consider this representative. Figure 5 (right) shows that IACT is close to or below one in all cases, indicating that the samples are approximately independent.

Figure 6 shows the posterior mean, 95% interquartile range, and 1D slices through the mean with 95% credibility interval. We see that the pipe layers are reconstructed well. However, the steel inclusions in the concrete layer are damped due to the prior, that promotes concrete's expected linear attenuation coefficient, which is lower than that of steel. We also note higher noise in the concrete layer than the remaining parts of the reconstruction due to $\delta_5 < \delta_{1,\dots,4}$. The 95% interquartile range is a direct reflection of the SGP prior. We see that imposing IID priors in the pipe layers lowers the uncertainty estimate of the posterior compared to areas without IID priors imposed. Furthermore, stronger priors with high precision lead to lower

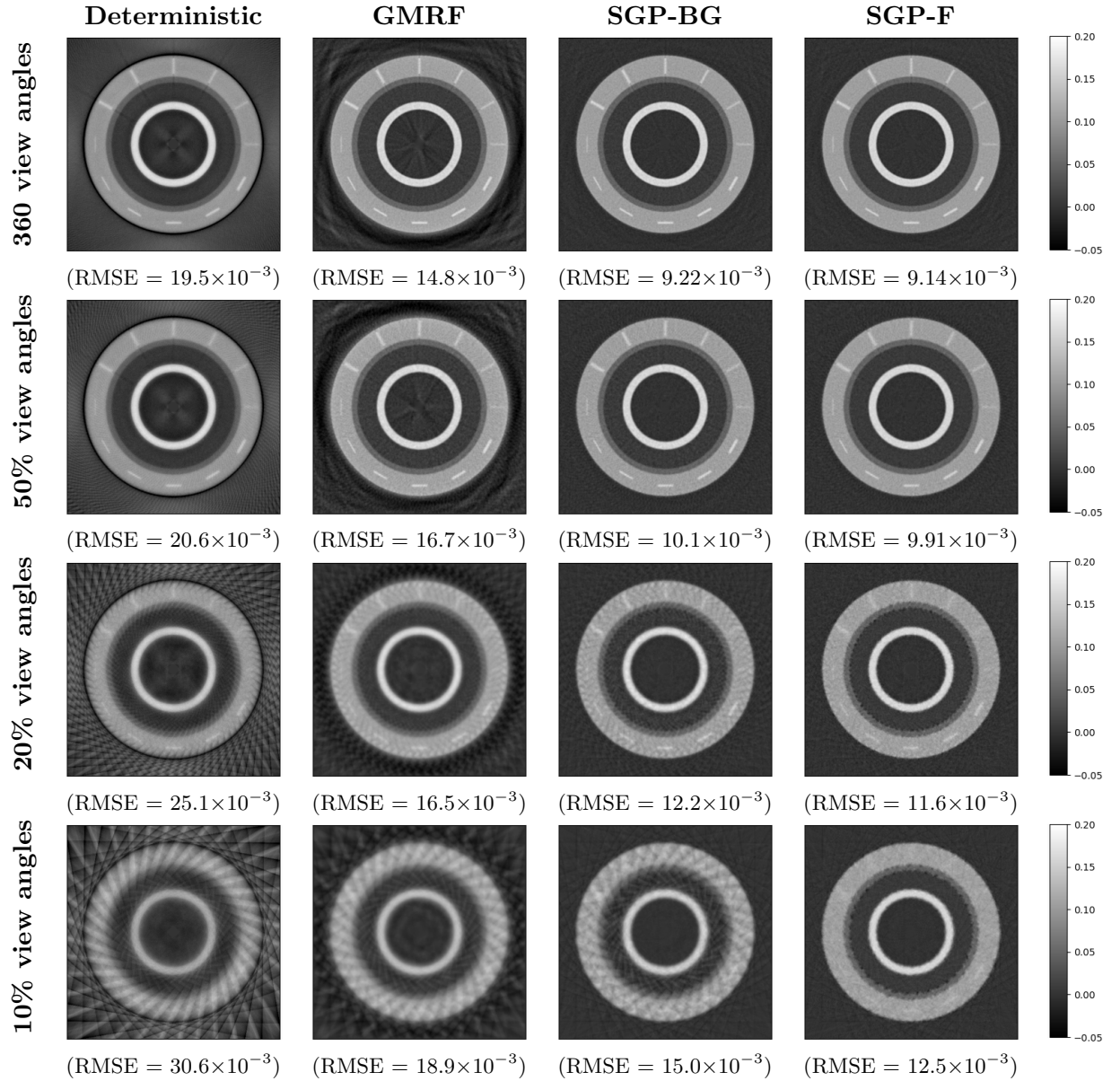


Figure 7. Posterior means and root-mean-square-error (RMSE) with increasingly informative SGPs (in columns) and decreasing number of view angles (in rows).

uncertainty. Finally, we see that the radial steel inclusions in the concrete layer are more difficult to reconstruct than the tangential inclusions as expected. For instance the 3 mm radial inclusion is barely distinguishable, while the 3 mm tangential inclusion is fairly clear.

5.3.2. Comparative study We investigate the effect of the SGP when reducing the number of view angles. Figure 7 shows posterior means in a grid, where the number of view angles is decreased across rows, and the prior information is increased across columns. We see, that as we add structural information, the reconstructions improve in terms of 1) reduced streak artifacts, 2) increased layer contrast, 3) reduced RMSE, and 4) steel inclusions that are hidden in artifacts appear when using structural information. The effect is especially clear for 10% and 20% view angles, indicating that the structural priors are more effective in sparse view angle cases.

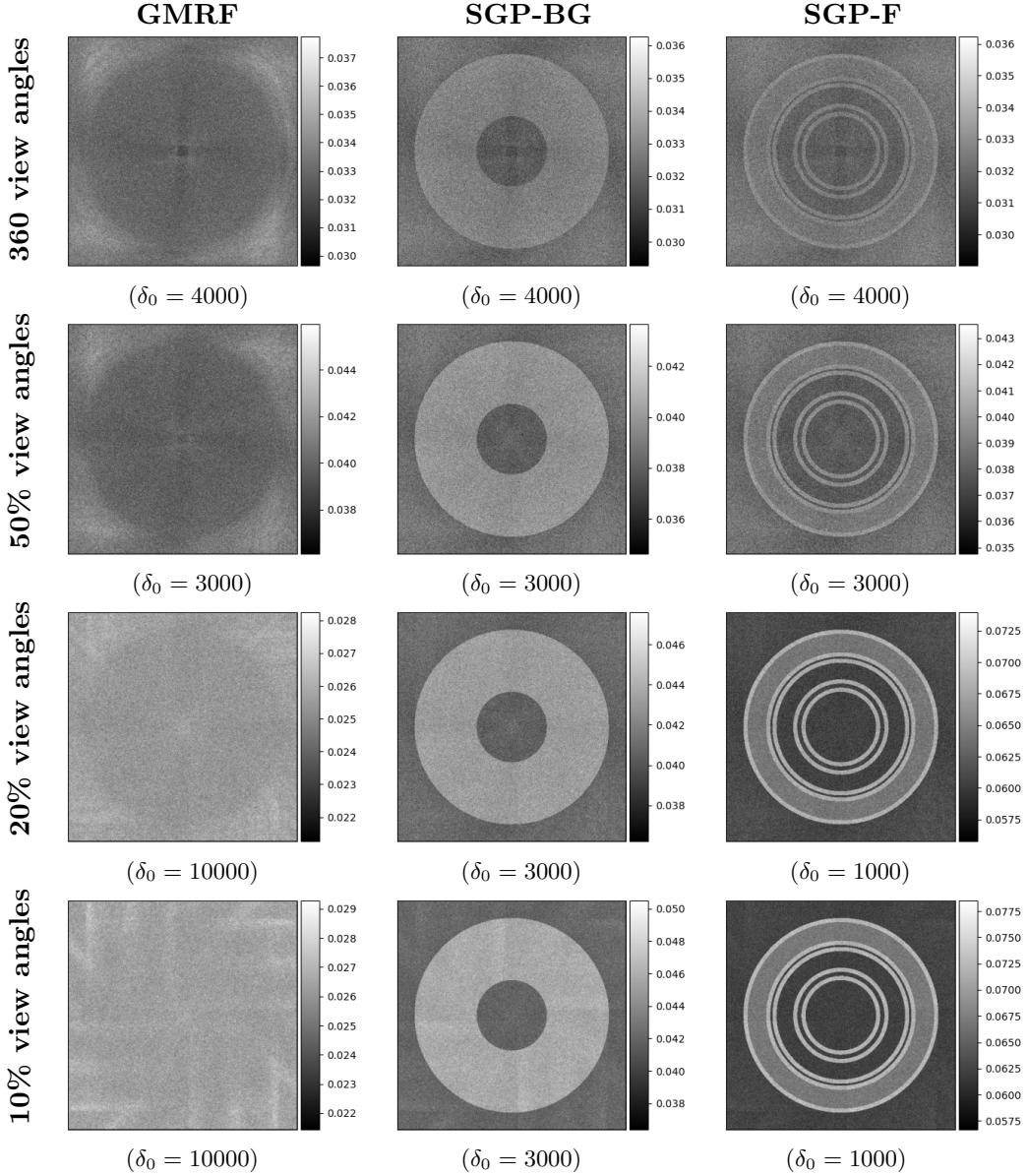


Figure 8. Posterior 95% interquantile range with increasingly informative SGPs (in columns) and decreasing number of view angles (in rows).

The deterministic reconstruction with 360 view angles produces an image where all the main features of the pipe are visible. However, we also see artifacts: 1) Along the radial steel inclusions, because these edges have no tangential rays, 2) in the centre of the image, because there is no data, and 3) a dark ring just outside of the pipe, which is a typical artifact that appears at the fan-beam edge. As we decrease the the number of view angles, we get more dominating artifacts from the fan-beam edges. When we add the GMRF prior, the artifacts are smoothed out, but still quite dominating in the image. Thus, this standard type prior is not sufficient to produce good reconstructions, especially for sparse view angles. Using the SGP-BG prior we reduce the artifacts in the background significantly. Furthermore, we see increased contrast between pipe materials. This effect is especially apparent for the 10% and 20% view angle cases. When we use the SGP-F prior we can suppress artifacts in the background and pipe layers. In the concrete

layer, however, we see the cost. Unexpected inclusions (here steel reinforcement), that are not accounted for in the prior, are also suppressed. Recall, that we did not impose any IID prior in boundary areas, and therefore the artifacts are not suppressed here, which we see as a “ragged” boundary, especially for sparse view angles.

We see that with the SGP-F prior we can resolve tangential steel inclusions down to widths of 2 mm using only 20% of the view angles. The radial inclusions are well reconstructed down to 4 mm. The 2-3 mm radial inclusions are visible, but faint and blurred. Compared to the deterministic reconstruction with no prior or to the reconstruction with GMRF prior, this is an improvement. In those cases, the narrow radial steel inclusions disappear among the artifacts. For the 10% view angles case, it becomes difficult to reconstruct any of the steel inclusions using any of the priors. Only the widest tangential inclusions appear faintly in the reconstructions.

In Figure 8, we show the 95% interquantile ranges of the posteriors, which we interpret as uncertainty estimates for the reconstructions. Note that the colorbars for the images are different. The GMRF prior yields an uncertainty pattern reflecting the acquisition geometry and corresponds to the structure of the likelihood. For the SGP priors the uncertainty pattern reflects the structure in the prior. For SGP-F, we observe lowest uncertainty in the background and in the steel, PU, and PE layers (regions 1-4), where we find the highest prior precision parameters. The concrete layer (region 5) has a lower prior precision, and thus a higher uncertainty. The highest uncertainty is found in the boundary regions, where no particular attenuation coefficient is promoted. We note that the boundary regions seem to have relatively higher uncertainty for 10% and 20% view angles, than for 50% and 100%. This is caused by the lower GMRF precision δ_0 for the two former cases. Finally, the likelihood structure is visible for the SGP-F prior cases with 50% and 100% view angles, but not with 10% and 20%. We suspect that this is due to the prior having a relatively larger influence than the likelihood, when there is sparse data.

5.4. Real data experiments

We now apply the SGPs to real data and obtain reconstructions with image qualities that appear comparable to the synthetic experiments. As for the synthetic data, we will study the effect of the SGP priors in combination with sparse view angles data. Figure 9 shows the posterior means in a grid, where the priors and number of view angles are varied. Our observations in the synthetic data experiments are in good agreement with the real data case. Again, we see dominating artifacts when decreasing the number of view angles in the deterministic reconstruction with no prior information. We also see, that they are reduced by introducing structural information. In the 20% view angles case, we see that the SGPs not only reduce artifacts, but also help increase contrast between materials. In the most extreme case, with only 10% view angles, we lose a lot of details in the reconstruction, such as the irregularities between the PU and PE layers. We do, however, still see traces of the large steel inclusion in the concrete layer.

In Figure 10, we see 95% interquantile ranges associated with the posteriors. Again, we see the acquisition geometry reflected, when using the GMRF prior, and the SGP structures reflected, when using those. Note that the steel rods used to fixate the pipe during measurements do not have any IID prior promoting a particular attenuation coefficient.

6. Discussion and Conclusions

We have proposed a method of introducing a-priori structural information in Bayesian CT reconstruction. Structural Gaussian priors are constructed based on well-known geometry and materials to promote expected attenuation coefficients in CT reconstructions. We applied the SGP in a case study of CT imaging of a subsea pipe with an offset fan-beam acquisition geometry. Numerical experiments with real and synthetic data showed that SGPs improve reconstructions, in terms of suppressed artifacts and enhanced contrast between materials, compared to traditional methods with no prior information or with a standard smoothing GMRF

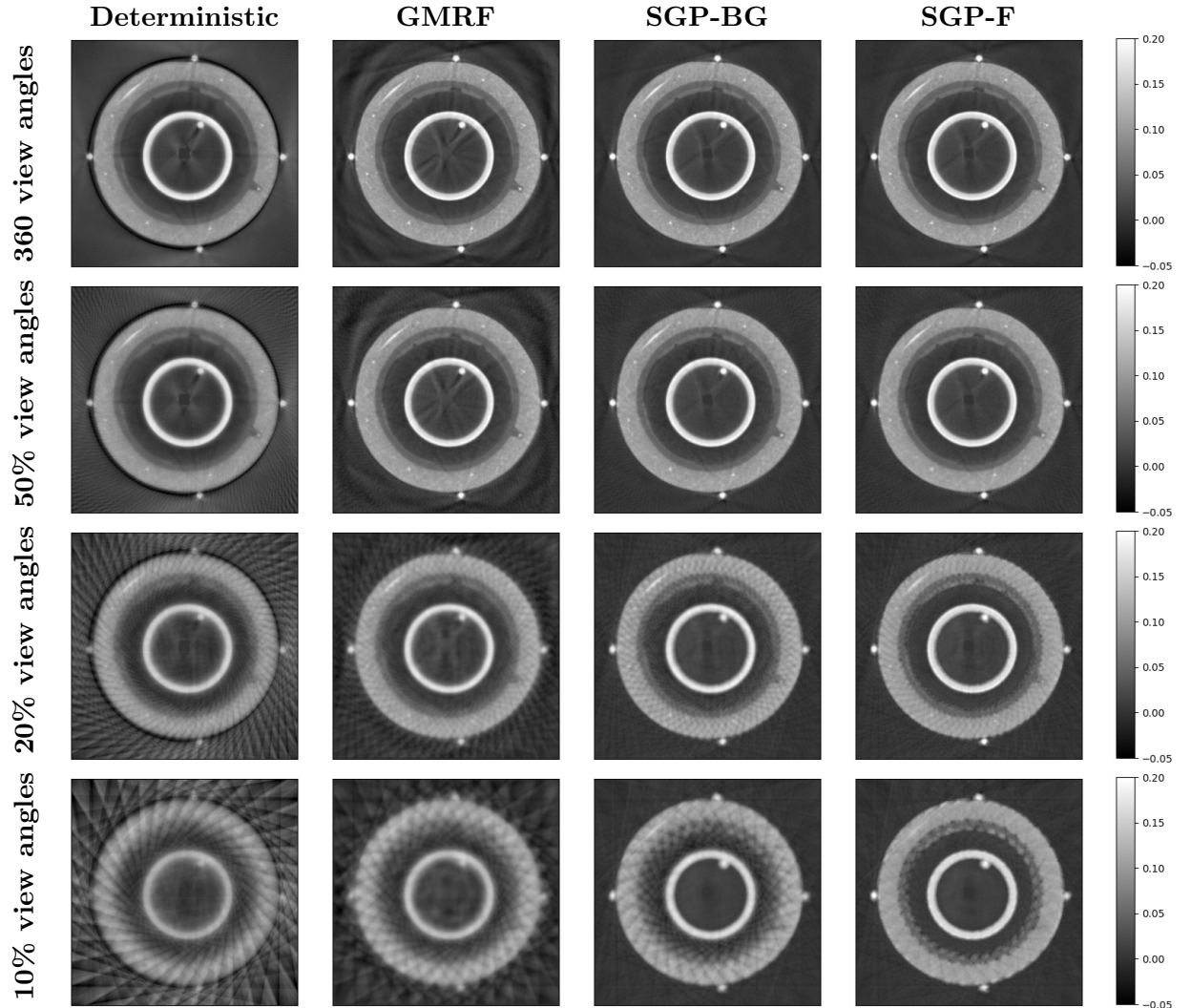


Figure 9. Posterior means with increasingly informative SGPs (in columns) and decreasing number of view angles (in rows).

prior. The SGPs were especially powerful in setups with sparse view angles. Information about all the pipe’s layers is required to construct the SGP-F. In some cases, we might only have access to the pipe’s exterior dimensions. The numerical results showed, that also here, imposing a SGP in the background resulted in significant improvements of the reconstructions.

As the posterior is Gaussian and defined in terms of square-root precision matrices, it can be efficiently sampled by solving a linear system of equations, yielding approximately independent samples. This is a useful property compared to conventional Markov chain Monte Carlo (MCMC) methods such as Metropolis Hastings [24] or more modern Hamiltonian MCMC methods [25], where independent samples can not be guaranteed.

If uncertainty estimates are not required, our method (with SGP priors) can also achieve reconstructions using MAP estimates, which can be computed extremely efficiently. However, since one of our main goals is uncertainty quantification, we chose to sample the posterior.

Interpretation of the posterior uncertainty estimates is difficult and requires more study. We observed that the GMRF prior gives rise to uncertainty estimates that reflect the acquisition geometry, which is in agreement with the results in [26]. When imposing the SGP, we noticed,

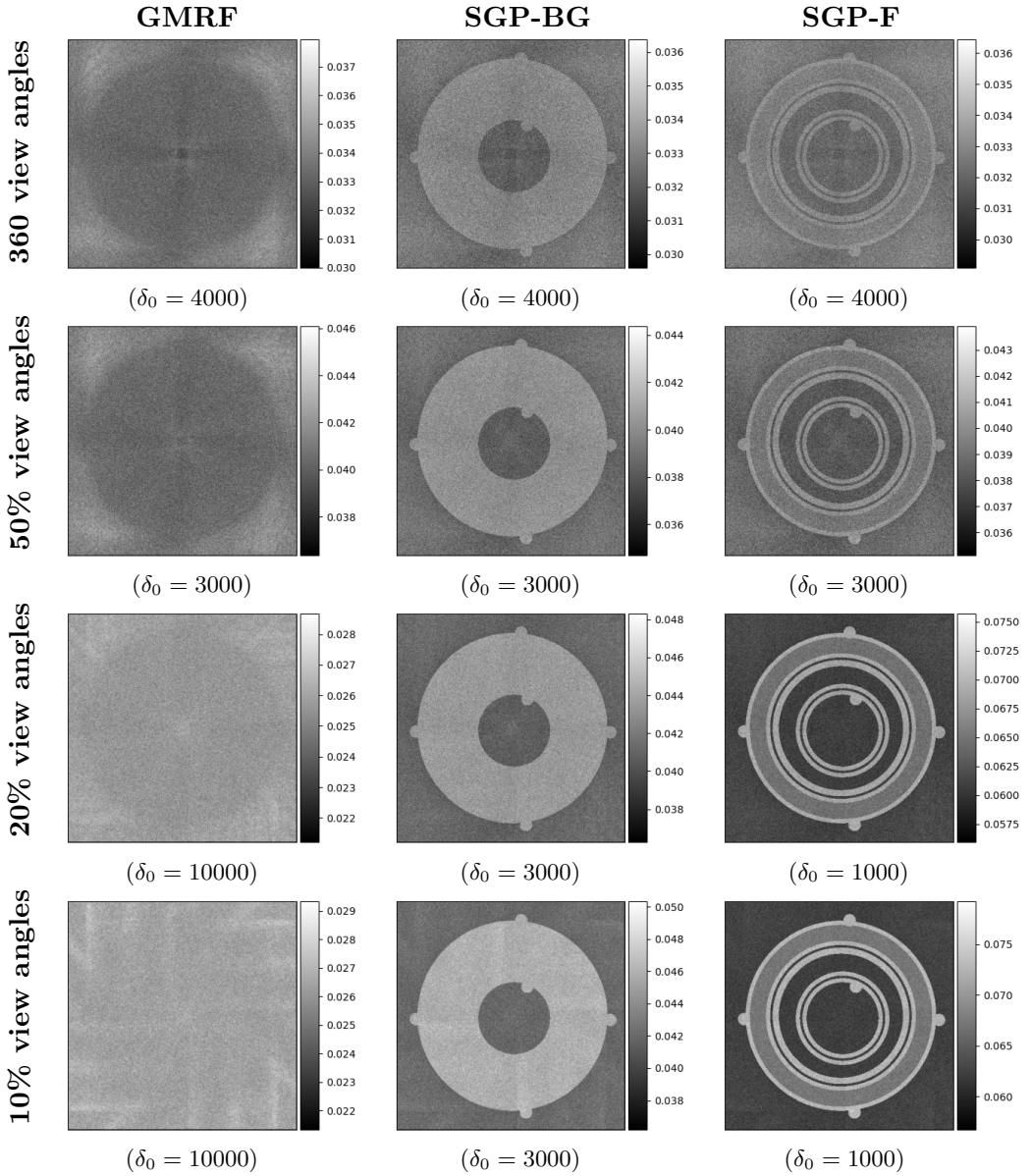


Figure 10. Real data: Posterior 95% interquantile range with increasingly informative SGPs (in columns) and decreasing number of view angles (in rows).

that the uncertainty estimates directly reflected the prior. The prior's effect on the uncertainty estimates have also been seen in other studies. For instance, edge-preserving priors give rise to high uncertainty on discontinuities in CT reconstructions [3, 4]. In future work we aim to further improve uncertainty estimates of the pipe and defect structure, for example to help distinguish artifacts from real features in the reconstruction.

Acknowledgments

This work was supported by The Villum Foundation (grant no. 25893). We also thank FORCE Technology for providing real data and information regarding subsea pipes.

References

- [1] Riis N A B, Frøsig J, Dong Y and Hansen P C 2018 Limited-data x-ray CT for underwater pipeline inspection *Inverse Problems* **34** 034002
- [2] Kaipio J and Somersalo E 2005 *Statistical and Computational Inverse Problems* (Dordrecht: Springer)
- [3] Suuronen J, Emzir M, Lasanen S, Särkkä S and Roininen L 2020 Enhancing industrial x-ray tomography by data-centric statistical methods *Data-Centric Engineering* **1** e10
- [4] Uribe F, Bardsley J, Dong Y, Hansen P C and Riis N 2021 A hybrid gibbs sampler for edge-preserving tomographic reconstruction with uncertain view angles (*Preprint arXiv:2104.06919*)
- [5] Hansen P C, Jørgensen J S and Lionheart W R B (eds) 2021 *Computed Tomography: Algorithms, Insight, and Just Enough Theory* (Philadelphia: SIAM)
- [6] Sidky E Y and Pan X 2008 Image reconstruction in circular cone-beam computed tomography by constrained, total-variation minimization *Physics in Medicine & Biology* **53** 4777
- [7] Bardsley J M 2018 *Uncertainty Quantification for Inverse Problems* (Philadelphia: SIAM)
- [8] Bardsley J M 2013 Gaussian Markov random field priors for inverse problems *Inverse Problems and Imaging* **7** 397–416
- [9] Bardsley J M 2012 Laplace-distributed increments, the laplace prior, and edge-preserving regularization *Journal of Inverse and Ill-Posed Problems* **20** 271–285
- [10] Markkanen M, Roininen L, Huttunen J M J and Lasanen S 2019 Cauchy difference priors for edge-preserving Bayesian inversion *Journal of Inverse and Ill-posed Problems* **27** 225–240
- [11] Zhang H, Han H, Ma J, Liu Y, Moore W and Liang Z 2014 Deriving adaptive MRF coefficients from previous normal-dose CT scan for low-dose image reconstruction via penalized weighted least-squares minimization *Medical physics* **41** 041916
- [12] Zhang H, Han H, Liang Z, Hu Y, Liu Y, Moore W, Ma J and Lu H 2016 Extracting information from previous full-dose CT scan for knowledge-based Bayesian reconstruction of current low-dose CT images *IEEE Transactions on Medical Imaging* **35** 860–870
- [13] Han H, Zhang H, Wei X, Moore W and Liang Z 2016 *Medical Imaging 2016: Physics of Medical Imaging* p 97834F
- [14] Gao Y, Liang Z, Moore W, Zhang H, Pomeroy M, Ferretti J, Bilfinger T, Ma J and Lu H 2019 A feasibility study of extracting tissue textures from a previous full-dose CT database as prior knowledge for Bayesian reconstruction of current low-dose CT images *IEEE Transactions on Medical Imaging* **38** 1981–1992
- [15] Fukuda W, Maeda S i, Kanemura A and Ishii S 2010 *2010 IEEE International Conference on Acoustics, Speech and Signal Processing* pp 2126–2129
- [16] Buzug T and Tomography C 2008 *From photon statistics to modern cone-beam CT* (Berlin: Springer)
- [17] Hubbell J H and Seltzer S M 2004 Tables of x-ray mass attenuation coefficients and mass energy-absorption coefficients (version 1.4) [Online] Available: <https://dx.doi.org/10.18434/T4D01F>. Accessed: 2021-01-19.
- [18] Rue H and Held L *Gaussian Markov Random Fields Theory and Applications* (New York: Chapman & Hall/CRC) ISBN 1-54488-432-0
- [19] Bickel P and Doksum K 2001 *Mathematical Statistics: Basic Ideas and Selected Topics*. 2nd ed vol 1 (New Jersey: Prentice Hall)
- [20] Björck A 1996 *Numerical Methods for Least Squares Problems* (Philadelphia: SIAM)
- [21] van Aarle W, Palenstijn W J, Cant J, Janssens E, Bleichrodt F, Dabravolski A, Beenhouwer J D, Batenburg K J and Sijbers J 2016 Fast and flexible x-ray tomography using the ASTRA toolbox *Opt. Express* **24** 25129–25147
- [22] van Aarle W, Palenstijn W J, De Beenhouwer J, Altantzis T, Bals S, Batenburg K J and Sijbers J 2015 The astra toolbox: A platform for advanced algorithm development in electron tomography *Ultramicroscopy* **157** 35–47 ISSN 0304-3991 URL <https://www.sciencedirect.com/science/article/pii/S0304399115001060>
- [23] Palenstijn W J, Batenburg K J and Sijbers J 2011 Performance improvements for iterative electron tomography reconstruction using graphics processing units (GPUs) *Journal of Structural Biology* **176** 250–253 ISSN 1047-8477
- [24] Hastings W K 1970 Monte carlo sampling methods using Markov chains and their applications *Biometrika* **57** 97–109
- [25] Duane S, Kennedy A, Pendleton B J and Roweth D 1987 Hybrid monte carlo *Physics Letters B* **195** 216–222 ISSN 0370-2693
- [26] Bardsley J M 2012 MCMC-based image reconstruction with uncertainty quantification *SIAM Journal on Scientific Computing* **34** A1316–A1332